Material identification in x-ray microscopy and micro CT using multi-layer, multi-color scintillation detectors

Dimple Modgil, David S. Rigie, Yuxin Wang*, Xianghui Xiao*, Phillip A. Vargas and Patrick J. La Rivière
*Department of Radiology, University of Chicago and *Advanced Photon Source, Argonne National Lab*

We demonstrate that a dual-layer, dual-color scintillator construct for microscopic CT, originally proposed to increase sensitivity in synchrotron imaging, can also be used to perform material quantification and classification when coupled with polychromatic illumination. We consider two different approaches to data handling: (1) a data-domain material decomposition whose estimation performance can be characterized by the Cramer-Rao Lower Bound formalism but which requires careful calibration and (2) an image-domain material classification approach that is more robust to calibration errors. The data-domain analysis indicates that useful levels of SNR (>5) could be achieved in one second or less at typical bending magnet fluxes for relatively large amounts of contrast (several mm path length, such as in a fluid flow experiment) and at typical undulator fluxes for small amount of contrast (tens of microns path length, such as an angiography experiment). The tools introduced could of course be used to study and optimize parameters for a wider range of potential applications. The image domain approach was analyzed in terms of its ability to distinguish different elemental stains by characterizing the angle between the lines traced out in a two-dimensional space of effective attenuation coefficient in the front and back layer images. This approach was implemented at a synchrotron and the results were consistent with simulation predictions.

I. INTRODUCTION

Synchrotron-based x-ray imaging is a powerful tool in biomedical research because it can produce micron-resolution, two- and three-dimensional images of small biological specimens. The direct detection of kilovoltage x-rays using pixelated solid-state detectors is not feasible at single-micron resolution [1–3]. Instead, x-rays impinge upon a thin, continuous scintillator and the resulting visible light emissions are focused onto a CCD using microscope optics. With this type of detector, sub-micron spatial resolution has been achieved [4]. The thickness of the scintillator must be matched to the depth of focus (DOF) of the microscope objective or the target resolution will not be achieved. With the push toward micron and submicron spatial resolution, this often constrains the scintillator thickness to be on the order of 5-50 microns. Despite being made of dense, high-Z materials, such thin scintillators invariably sacrifice absorption efficiency in order to achieve spatial resolution.

To overcome this problem, Martin *et al.* explored using two scintillator layers, each doped differently so as to emit a different wavelength of optical light (specifically, they used LSO:Tb, with peak emission at 550nm and and LYSO:Ce, with peak emission at 420 nm) [5]. A dichroic mirror separated the emission spectra and they were directed to two different lens-CCD systems. Since each lens received emissions from only one layer, its DOF needed only match the thickness of that layer, not both layers, and thus the total scintillator thickness could be doubled with little resolution degradation.

While Martin *et al.* introduced such multi-layer scintillators to improve detection efficiency in the context of monochromatic x-ray illumination, a very similar construct could be used in combination with polychromatic illumination in order to perform energy-resolved detection. In the case of polychromatic illumination, the first layer will preferentially stop lower-energy x-rays, and the deeper layers higher-energy x-rays, leading to limited but perfectly registered spectral resolution. This is conceptually similar to the dual-layer detectors investigated for use in clinical radiography and CT [6–9]. In the case of human CT, fast kV switching, the use of multiple tubes, and emerging photon-counting detectors provide alternative means of acquiring x-ray spectral information[10], but these technologies are not feasible for synchotron micro CT. While it is of course possible to perform spectral imaging at synchrotrons by acquiring images at multiple monochromatic energies, the monochromatizing process greatly reduces the flux, which is especially problematic for dynamic studies. Moreover, changing beam energy is relatively slow (on the order of seconds), which further precludes the use of energy switching in dynamic studies.

In this paper, we analyze two approaches to using multi-layer scintillators for spectral imaging. The first follows the model of Martin *et al.*, using dichroic mirrors to parse the emissions into separate optical channels that are focused on the various layers. The second involves using a single optical channel coupled to a color-sensitive CCD. This second configuration is simpler but entails two tradeoffs. First, the detected signals in the CCD's RGB color channels need to demultiplexed and mapped back to the scintillator layer. This process has the potential to amplify noise, although careful choice of the scintillator emission spectra can greatly mitigate this effect. Second, the use of a single optical channel sacrifices the absorption efficiency gain that inspired the multi-layer scintillator in the first place; in the case of a single optical channel, the total thickness of all the layers needs to be matched to the DOF of the single objective lens.

We will investigate two approaches to analyzing the information obtained from the multi-layer scintillator configurations; these are analogous to the two most common approaches used in spectral CT. The first seeks to perform quantitative material decomposition in the projection data domain, assuming the object is comprised of known basis materials of unknown spatial distribution[11]. The resulting material sinograms can be used to solve for material density maps. This approach is quantitative

and, building on work by Roessl *et al.*[12], we use the Cramer-Rao lower bound (CRLB) formalism to determine potential material sensitivity and optimize acquisition parameters. However, this material quantification approach requires accurate knowledge or calibration of system parameters such as the incident spectrum and detector responses. An alternative approach seeks simply to classify pixels in reconstructed images as belonging to a particular material. This can be achieved by reconstructing the data from the various scintillator layers separately and performing classification in the resulting multidimensional attenuation space [13]. We model this approach for various combination of scintillator materials and thickness and predict the classification performance for pairs of metal-based stains. We also perform a synchrotron-based experiment to demonstrate the feasibility of this approach and to validate the predictions.

This paper builds on previously presented preliminary results but contains a more thorough and accurate model of the optical components as well as a much more complete analysis of the potential sensitivity of the approach[14, 15].

II. METHODS

A. Background on scintillator-microscope MicroCT

A basic schematic of conventional synchrotron-based micro CT detection is shown in Fig. 1(Top).

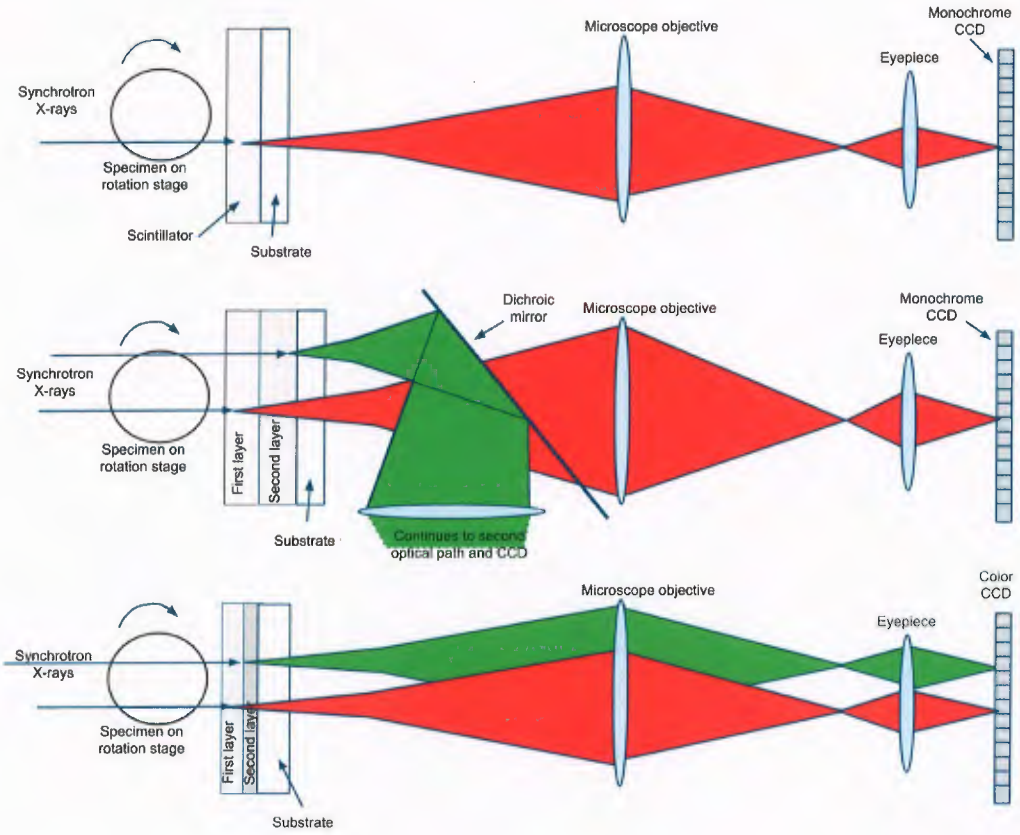

Figure 1: Schematic illustrating standard and proposed synchrotron-based micro CT detection schemes. (Top) A standard synchrotron x-ray microscopy configuration, where a single layer scintillator converts x-ray flux into an optical image that is viewed with a microscope objective. (Center) Scheme proposed by Martin *et al.* for doubling effective scintillator thickness by using two layers emitting different colors of light that can be directed into two optical channels. In this paper, we explore the use of the setup with polychromatic illumination for material quantification and classification. (Bottom) An alternative scheme using a single optical channel and color camera to view a dual-layer dual-color scintillator. Note that the combined thickness of the layers must not exceed the depth of focus of the single microscope objective whereas for the two-channel scheme, each layer can satisfy that constraint individually.

The incident x-rays are effectively parallel since in a synchrotron the source is distant and the beam divergence is very small. The x-rays are transmitted through the object with attenuation governed by standard considerations. The x-rays interact in the

thin scintillating screen, which is typically made from a high-density, high-Z scintillator such as LSO, LYSO, or YAG doped with an appropriate impurity such as Tb or Ce. The active portion of the scintillator rests on a structural substrate, often just the same material without the doping. The scintillator converts the x-ray fluence into an optical image, which is magnified with a high numerical aperture microscope objective and focused on a CCD through an eyepiece. The spatial resolution is determined primarily by the numerical aperture of the lens, but can be degraded if out-of-focus light from the scintillator reaches the CCD. For this reason, the doped scintillator thickness must be well matched to the depth of focus of the objective lens. Koch *et al.* have carefully analyzed the resolution achievable in such systems, accounting also for diffraction and spherical aberration effects, and found that the full width half maximum (FWHM) of the point spread function, which we denote R_{50} and measure in microns, can be predicted by the following empirical equation

$$R_{50} = \sqrt{\left(\frac{p}{NA}\right)^2 + (qzNA)^2}, \tag{1}$$

where $p = 0.18$ and $q = 0.075$ are empirically determined constants, and z is the thickness of the doped scintillator in microns [4]. For a lens of given NA, this equation can be used to determine the maximum scintillator thickness z, which we denote z_{max}, that is compatible with a specified resolution R_{50}. For example, for a 5X lens with NA = 0.127, achieving an R_{50} resolution of 1.5 microns requires a scintillator with $z_{max} \leq 50$ microns.

B. Material decomposition using multi-layer scintillator with multiple optical channels

We now consider the generalization of this approach to a multi-layer scintillator with different dopants in each layer. Figure 1(center) depicts the schematic of a dual-layer setup. A polychromatic beam of x-rays is incident on the object and is attenuated according to standard considerations. As depicted, the x-rays that are absorbed in the first layer lead to emission of primarily green light and the x-rays that interact in the second layer lead to emission of primarily red light. (In practice, the emission spectra of the different layers are determined by the dopant and are a design parameter.) A dichroic mirror allows the emissions from the first layer to pass through into an optical channel comprising an objective lens, an eyepiece, and a monochrome CCD. The same dichroic mirror redirects the emissions from the second layer into a second optical channel comprising an objective lens, an eyepiece, and a monochrome CCD. Because the lower energy x-rays are preferentially attenuated in the first layer, the signals from the two layers encode spectral information that can be used to perform quantitative material decomposition using the model to be developed below. The essential features of the model derive from similar analyses of dual-energy CT and dual-layer CT detectors[11, 12] but the details are specific to the scintillator-microscope configuration.

1. Model

Let $I_0(E)$ denote the polyenergetic X-ray fluence rate incident on the specimen, in photons cm^2 s^{-1} keV^{-1}, where E denotes energy in keV. The specimen will attenuate the incident X-ray beam and modify the spectrum. The specimen is described by an energy-dependent attenuation map $\mu(\mathbf{x},E)$, where μ has units of inverse length and $\mathbf{x}$ is a spatial coordinate vector.

The modified fluence spectrum $I(E)$ as transmitted along line L is then related to the incident X- ray fluence spectrum $I_0(E)$ by:

$$I(E) = I_0(E)\exp\left(-\int_L \mu(\mathbf{x},E)dl\right). \tag{2}$$

We assume the specimen comprises a finite number N_{mat} of known "basis materials" of unknown spatial distribution. These could be soft tissue, and a high-Z contrast material, for example. The attenuation map can then be expressed as $\mu(\mathbf{x},E) = \sum_{k=1}^{N_{mat}} a_k(\mathbf{x}) f_k(E)$. Here $a_k(\mathbf{x})$ is the spatial density distribution of material k in g/cm^3 and $f_k(E) \equiv \left(\frac{\mu}{\rho}\right)_k(E)$ is the energy-dependent mass-attenuation coefficient of material k in cm^2/g. These mass-attenuation coefficients are known quantities that are tabulated by, for example, NIST [16]. Substituting this expression for $\mu(\mathbf{x},E)$ and rearranging yields

$$I(E) = I_0(E)\exp\left(-\sum_{k=1}^{N_{mat}} f_k(E)\int_L a_k(\mathbf{x})dl\right). \tag{3}$$

Finally, we define

$$A_k \equiv \int_L a_k(\mathbf{x}),$$

representing the line integral through the density distribution of material k. Given a complete set of such line integrals through a given material basis function, it is possible to perform tomographic reconstruction of the density distribution $a_k(\mathbf{x})$ using standard tomographic reconstruction algorithms. The vector $\mathbf{A} = (A_1, ..., A_{N_{mat}})$ represents the set of unknown material line integrals for a given line through the object. We can then rewrite Eqn. 3, making explicit the dependence on the vector $\mathbf{A}$.

$$I(E;\mathbf{A}) = I_0(E)\exp\left(-\sum_{k=1}^{N_{mat}} f_k(E)A_k\right). \tag{4}$$

In practice, we cannot measure line integrals of infinitesimal width, but rather of finite size corresponding to the size of a CCD detector pixel mapped onto the continuous scintillator. We assume this virtual scintillator pixel, which we call a detection pixel, has side w and area w^2.

In this section, we focus our analysis on the problem of solving for the vector of unknown material line integrals using the spectral energy information encoded in the layer interactions for a single detection pixel. The number of x-rays absorbed in a detection pixel in layer i of the detector during a time interval τ seconds is given by

$$N_i^{det}(E;\mathbf{A}) = w^2\tau I(E;\mathbf{A})D_i(E), \tag{5}$$

where $D_i(E)$ is the probability a photon of energy E is detected in layer i. The detection probability for a given layer depends on the attenuation and thickness of the overlying layers as well as those of the layer itself, and it is given by

$$D_i(E) = \left(1 - e^{-\mu_i(E)t_i}\right)\sum_{i'=1}^{i-1} e^{-\mu_{i'}(E)t_{i'}}, \tag{6}$$

where $\mu_i(E)$ and t_i are the linear attenuation coefficient and thickness of layer i, respectively.

Each detected x-ray in a given layer leads to emission of optical scintillation photons in proportion to its energy, with constant of proportionality $\eta_i^{x/v}$ (i.e., $\eta_i^{x/v}$ is the energy conversion efficiency of x-rays to visible light). For a given dopant, the optical photons have a spectrum, $S_i(\lambda)$, generally narrowly peaked. Overall, the number of optical photons of wavelength λ emitted by layer i is given by

$$N_i^{opt}(\lambda;\mathbf{A}) = \eta_i^{x/v}S_i(\lambda)\int N_i^{det}(E;\mathbf{A})EdE. \tag{7}$$

We assume that the dichroic mirror and appropriate filters are able to perfectly separate the spectra from the two layers into the two optical channels. The emissions of layer i are magnified by the objective lens in optical channel i, which has collection efficiency $\eta_i^{coll} = \frac{1}{4}\left(\frac{NA}{n_i}\right)^2$, where NA is the lens numerical aperture and n is the index of refraction of the scintillator. The emissions are then focused onto the ith monochromatic CCD which has spectral response $R_i^{mono}(\lambda)$, yielding a measurement

$$\overline{M}_i(\mathbf{A}) = \eta_i^{coll}\int N_i^{opt}(\lambda;\mathbf{A})R_i^{mono}(\lambda)d\lambda. \tag{8}$$

We have used an overbar to signal that this is the expected value of a random variable. We will consider noise properties in the next section. Substituting Eqn. 7 and rearranging yields

$$\overline{M}_i(\mathbf{A}) = \eta_i^{coll}\eta_i^{x/v}\int N_i^{det}(E;\mathbf{A})EdE\int S_i(\lambda)R_i^{mono}(\lambda)d\lambda. \tag{9}$$

The last integral is the quantum efficiency of the CCD for the emissions of the ith scintillator layer and we denote it

$$\eta_i^{v/e} \equiv \int S_i(\lambda)R_i^{mono}(\lambda)d\lambda.$$

So the final expression for the mean measurement is

$$\overline{M}_i(\mathbf{A}) = \eta_i^{tot}\int N_i^{det}(E;\mathbf{A})EdE, \tag{10}$$

where we have introduced $\eta_i^{tot} \equiv \eta_i^{coll}\eta_i^{v/e}\eta_i^{x/v}$.

2. Noise model

We assume that there are two principal sources of noise in the measurement: Poissonian photon-counting statistics governing the number of x-rays actually absorbed in the layer i and additive zero-mean Gaussian electronic noise with variance σ_e^2 in the CCD. The energy-weighting implicit in the conversion from polychromatic x-rays to optical photons means the resulting measurement is no longer strictly Poisson, but rather compound Poisson[17–19]. The sum of a compound Poisson and Gaussian distributions does not yield a tractable statistical likelihood function so we approximate the sum as a Gaussian with mean and variance matching the first two moments of the actual distribution. As long as the number of detected x-rays per channel exceeds 10 or so, this is likely to be an excellent approximation. We also assume that the measurements in the two optical channels are statistically independent.

Overall then, we assume the measurement vector for a given detector pixel, $\mathbf{M} = \left(M_1, ..., M_{N_{lay}}\right)$ is multivariate normal, with means given by Eqn. 10 and a diagonal covariance matrix with the diagonal elements given by

$$\sigma_i^2(\mathbf{A}) = \left(\eta_i^{tot}\right)^2 \int N_i^{det}(E;\mathbf{A})\, E^2 dE + \sigma_e^2. \tag{11}$$

3. Solving for A

In the previous section, we developed a model that represents the measurements $\mathbf{M}$ in the N_{lay} optical channels as a system of nonlinear equations in terms of the N_{mat} unknown material $\mathbf{A}$. This can be seen explicitly by substituting Eqns. 5 and 4 into Eqn. 10:

$$\overline{M}_i(\mathbf{A}) = \eta_i^{tot} w^2 \tau \int I_0(E) \exp\left(-\sum_{k=1}^{N_{mat}} f_k(E) A_k\right) D_i(E) E dE, \tag{12}$$

There are a variety of potential approaches to solve the nonlinear system of equations for the elements of the vector $\mathbf{A}$ given the vector of measurements $\mathbf{M}$. In the original paper on dual-energy CT, Alvarez and Macovski proposed a polynomial expansion of the log of the measurements in terms of the elements of $\mathbf{A}$, with coefficients determined through calibration and the solution obtained numerically by means of a generalization of the Newton-Raphson method[11].

An alternative approach is to use a maximum-likelihood strategy. Given the noise model developed in the previous section, the negative log likelihood is given by

$$\mathscr{L}(\mathbf{A}) = \sum_{i=1}^{N_{lay}} \frac{\left[M_i - \overline{M}_i(\mathbf{A})\right]^2}{\sigma_i^2(\mathbf{A})} + \frac{1}{2} \ln \sigma_i^2(\mathbf{A}) \tag{13}$$

A variety of iterative methods could be applied to find the $\mathbf{A}$ minimizing this objective function[20–22] but our interest in this paper is in characterizing the best possible performance achievable by any such unbiased estimator. This is discussed in the next section.

4. CRLB

The use of maximum likelihood (ML) estimators for $\mathbf{A}$ is appealing because ML estimators are known to saturate the Cramer-Rao lower bound (CRLB) on unbiased estimator variance in cases when such an efficient estimator exists[23]. The CRLB formalism thus allows us to predict material decomposition performance as a function of various imaging parameters (such as beam intensity and time) and also allows us to optimize system design features (such as the scintillator material combinations and thicknesses). In our context, the CRLB states that the variance of the kth material line integral estimate will be greater than or equal to the kth diagonal element of the inverse Fisher information matrix.

$$\sigma_{A_k}^2 \geq \mathscr{F}_{\mathrm{kk}}^{-1} \tag{14}$$

where, as shown in Roessl[12] for uncorrelated Gaussian noise, $\mathscr{F}^{-1}$ is the inverse of the matrix with elements:

$$\mathscr{F}_{\alpha\beta} = E\left[-\frac{\partial^2 \mathscr{L}}{\partial A_\alpha \partial A_\beta}\right] \tag{15}$$

$$= \sum_{i=1}^{N_{lay}} \frac{1}{\sigma_i^2} \frac{\partial \overline{M}_i}{\partial A_\alpha} \frac{\partial \overline{M}_i}{\partial A_\beta} + \frac{1}{2} \sum_{i=1}^{N_{lay}} \frac{1}{\left(\sigma_i^2\right)^2} \frac{\partial \sigma_i^2}{\partial A_\alpha} \frac{\partial \sigma_i^2}{\partial A_\beta}. \tag{16}$$

5. *Use of CRLB to determine sensitivity and optimize parameters*

We use the CRLB formalism to perform a preliminary investigation of the potential accuracy of the dual-layer scintillator construct for contrast-agent quantification. The two scintillator layers are LYSO:Ce (front) and LuAG:Ce (rear) and the assumed imaging parameters are specified in Table I. We assume a target resolution of 1.5 μ, which constrains maximum layer thickness to 50 μ.

Parameter	Value
$I_0(E)$	Shown in Fig. 2 [photons/ (s cm^{2}10 eV)].
τ	1 s
w^2	2.25×10^{-8} cm^2
NA	0.127
n	1.81 for LYSO:Ce and 1.84 for LuAG:Ce
$\eta_i^{x/v}$	20 ph/keV for LuAG:Ce and 32 for LYSO:Ce
$\eta_i^{v/e}$	0.7
σ_e^2	5 electrons
$S_i(\lambda)$	Shown in Fig. ??

Table I: Imaging parameters

Synchrotron facilities typically contain two types of beamlines, bending magnets, located at the bends in the electron storage ring, and undulators, located along the straight segments. The flux at undulator beamlines is typically much higher than that at bending magnet beamlines and the spectrum comprises fairly narrow spikes at a range of harmonics. The bending magnet and undulator spectra assumed in all studies are shown in Fig. 2. They were generated using XOP[24] and have been converted from units of fluence rate (photons/s/cm^2) per fractional energy bandwidth to units of fluence rate per fixed 10 eV energy bin.

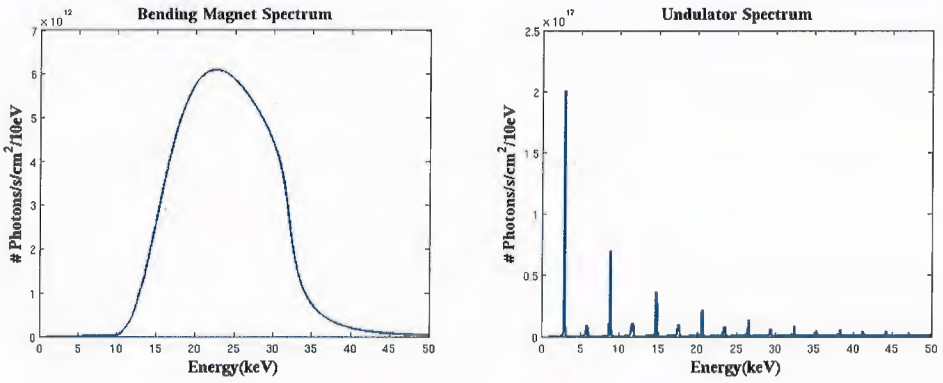

Figure 2: Synchrotron spectra assumed in studies

For these two-channel studies, the second scintillator layer thickness was fixed at 50 microns (the maximum compatible with the specified resolution requirement) and the first layer thickness was varied to yield the optimal SNR.

We simulated two different contrast-containing test objects. In both cases, we considered aqueous contrast solutions comprising 0.02 g/cm^3 Ag, I, W, Mo, or In, since these elements have K or L edges in the energy range of interest.

1. The first object seeks to simulate a single-view biological angiographic examination with the task being to quantify the amount of contrast agent in a 50 micron vessel contained in 3 mm of water-equivalent tissue. So the line integral through the small contrast-fileld vessel is A_α=10^{-4} g/cm^2 and the line integral through the larger background cylinder is A_β= 0.3 g/cm^2.

2. The second seeks to simulate a fluid flow/porosity experiment where a contrast agent is flowed through a porous sand column. In this case, we assumed the line of interest passed through 3 mm of SiO_2 and 3 mm of contrast solution. So A_α= 0.006 g/cm^2 for contrast and A_β= 0.3 g/cm^{2}for the background.

Recall that in this paper we are focused on the problem of estimating material line integrals for a single line integral. In both cases, we used the CRLB formalism to determine the lowest achievable variance in the estimate of the contrast material line

integral $\hat{\sigma}^2_{A_\alpha}$. We then define the SNR of the line integral estimate to be

$$SNR = \frac{A_\alpha}{\sqrt{\hat{\sigma}^2_{A_\alpha}}}.$$

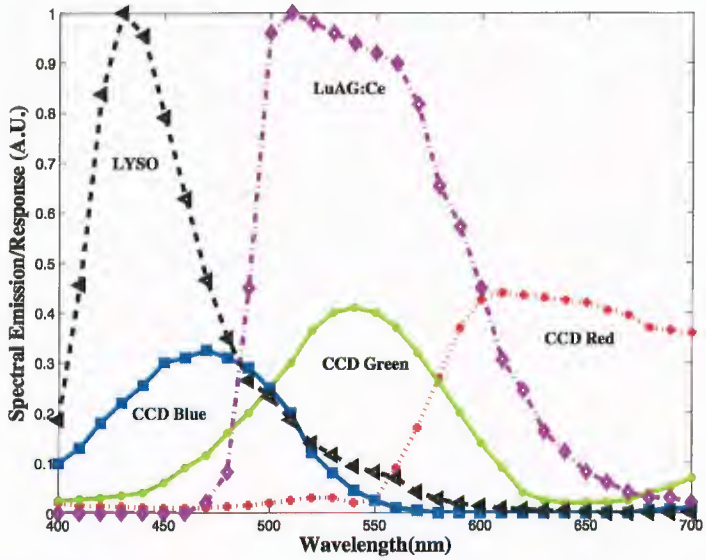

Figure 3: Emission spectra $S_i(\lambda)$of LuAG:Ce and LYSO and spectral response $R^C_j(\lambda)$for the RGB channels of the color camera. Note that the emission spectra $S_i(\lambda)$ have been normalized to have peak value 1 in order to improve readability of this plot. In practice, they are normalized to have area 1.

C. The results are presented in section III A.Material decomposition using multi-layer scintillator with single, color-sensitive optical channel

An alternative approach using a single optical channel is shown in Fig. 1(bottom). The key difference is the absence of a dichroic mirror and the use of a color CCD. This introduces two main challenges. First, the total thickness of the scintillator layers must be matched to the DOF of the objective lens, which will reduce overall absorption efficiency. Second, the signals from the various layers are not cleanly separated by the use of a dichroic mirror, but rather have the potential to be multiplexed in the color image recorded by the CCD.

1. Model

The chain of analysis remains the same through Eqn. 7. Beyond this point we have a single objective lens with collection efficiency η_i^{coll} focusing the light from all the layers onto a color CCD (the collection efficiency retains its layer index i, despite the use of a single lens, because the different layers could have different indices of refraction, although in practice they should be very closely matched to avoid reflection and refraction between layers). We assume the CCD color channels have response $G^C_j R^C_j(\lambda)$, where $j = 1,2,3$ correspond to the red, green, and blue channels, respectively. The constant G^C_j factors represent the Bayer filter fractions, which we model as 0.5 for the green channel and 0.25 for the red and blue channels. The color channel response functions$R^C_j(\lambda)$ that we assume are shown in Fig. **??** along with the emission spectra of the scintillating materials. So now we have

$$\overline{M}^C_j(\mathbf{A}) = \int \left[\sum_{i=1}^{N_{lay}} \eta_i^{coll} N_i^{opt}(\lambda;\mathbf{A})\right] G^C_j R^C_j(\lambda)\, d\lambda \tag{17}$$

$$= \int \left[\sum_{i=1}^{N_{lay}} \eta_i^{coll} \eta_i^{x/v} S_i(\lambda) \int N_i^{det}(E;\mathbf{A}) E dE \right] G_j^C R_j^C(\lambda) d\lambda \tag{18}$$

$$= \left[\sum_{i=1}^{N_{lay}} \int \eta_i^{coll} \eta_i^{x/v} N_i^{det}(E;\mathbf{A}) E dE \right] \int S_i(\lambda) G_j^C R_j^C(\lambda) d\lambda. \tag{19}$$

The final integral is the sensitivity of the jth color channel of the CCD to the emissions of the ith layer of the scintillator and we can write it as elements of a matrix B:

$$B_{ji} \equiv G_j^C \int S_i(\lambda) R_j^C(\lambda) d\lambda. \tag{20}$$

Thus we have

$$\overline{M}_j^C(\mathbf{A}) = \sum_{i=1}^{N_{lay}} B_{ij} \eta_i^{x/v} \eta_i^{coll} \int N_i^{det}(E;\mathbf{A}) E dE. \tag{21}$$

If we define a vector $\mathbf{N}^{tot}(\mathbf{A})$ with elements

$$N_i^{tot}(\mathbf{A}) \equiv \eta_i^{x/v} \eta_i^{coll} \int N_i^{det}(E;\mathbf{A}) E dE, \tag{22}$$

corresponding to the total number of optical photons emitted by layer i and incident on the camera, then we can reexpress Eqn. 21 as a matrix equation

$$\overline{\mathbf{M}}^C = B\mathbf{N}^{tot}(\mathbf{A}). \tag{23}$$

2. *Noise, Likelihood, and CRLB*

The two key sources of noise are again assumed to be photon-counting noise related to the initial x-ray detection in each layer as well as additive Gaussian noise in the CCD. However, the mixing of signals from the different layers in the color detection step leads to noise correlation that must be accounted for in solving the equations and in the CRLB analysis. We still assume the measurement vector is multivariate normal, and the mean is given by Eqn. 23.

We can determine the covariance matrix by considering that vector $\mathbf{N}^{tot}(\mathbf{A})$ has diagonal covariance matrix C^{tot} given by

$$C^{tot} = Diag\left\{ \left(\eta_i^{x/v} \eta_i^{coll} \right)^2 \int N_i^{det}(E;\mathbf{A}) E^2 dE \right\}.$$

Then using standard rules for the effect of linear transformation on covariance and adding the effect of uncorrelated electronic noise, we have

$$C = BC^{tot}B^T + \sigma_e^2 I. \tag{24}$$

Again, a maximum likelihood solution for $\mathbf{A}$ is likely to have desirable properties. In the presence of measurement covariance, the negative log-likelihood function is now given by

$$\mathscr{L}(\mathbf{A}) = \left[\mathbf{M}^C - \overline{\mathbf{M}}^C(\mathbf{A}) \right]^T C^{-1} \left[\mathbf{M}^C - \overline{\mathbf{M}}^C(\mathbf{A}) \right] + \frac{1}{2} \ln\left[|C| \right]. \tag{25}$$

Finally, we will again make use of the CRLB formalism. However, a different expression for the Fisher information matrix must be used when there is covariance among the measurements [23]. It is given by:

$$F_{\alpha\beta} = \left[\frac{\partial \overline{\mathbf{M}}^C}{\partial A_\alpha} \right]^T C^{-1} \left[\frac{\partial \overline{\mathbf{M}}^C}{\partial A_\beta} \right] + \frac{1}{2} Tr\left[C^{-1} \frac{\partial C}{\partial A_\alpha} C^{-1} \frac{\partial C}{\partial A_\beta} \right]. \tag{26}$$

3. Use of CRLB to determine sensitivity and optimize parameters

We again use the CRLB formalism to determine the achievable contrast material line integral estimator SNR for the same test objects as were used in the two optical channel case. One key difference is that to meet the resolution targets, the sum of the two scintillator layer thickness may not exceed 50 microns, so we considered all possible combinations of layer thickness in 5 micron increments to identify the combination yielding the optimal contrast material line integral SNR. The results are presented in section III A.

D. Material classification using multi-layer scintillators

1. Approach

The preceding approaches for quantitative material decomposition require accurate knowledge or calibration of the x-ray spectrum and detector spectral responses. An alternative approach, widely used in dual-energy CT, seeks instead to reconstruct images from the different spectral channels independently and to then perform an image-domain material classification[10, 13]. In the case of dual-energy CT, each pixel location then has a pair of attenuation values associated with it: a low-energy weighted one and a high-energy weighted one. When viewed on a scatter plot of pixel values in the resulting two-dimensional attenuation coefficient space, different materials often occupy characteristic sloped lines. The distance along the line is determined by the concentration of the material. In the case of two materials (typically the most one can hope to distinguish from two spectral measurements), the angle between the lines provides some measure of the system material separability.

In the case of the layered scintillator with multiple optical channels, we achieve this as follows. We normalize the signal from each layer by the corresponding blank scan signal from that layer (i.e., the signal acquired in the absence of an absorbing object). We then take the negative logarithm in order to obtain an approximate estimate of the energy-weighted line integral. Specifically, we define new measurements as

$$P_i \equiv -\ln\left(\frac{M_i(\mathbf{A})}{M_i(\mathbf{0})}\right).$$

Substituting for M_i and canceling common factors we obtain

$$P_i = -\ln\left[\frac{\int I_0(E)\exp\left(-\int_L \mu(\mathbf{x},E)dl\right)D_i(E)EdE}{\int I_0(E)D_i(E)EdE}\right].$$

Defining an energy weighting term,

$$w_i(E) = \frac{I_0(E)D_i(E)E}{\int I_0(E)D_i(E)EdE}, \tag{27}$$

we have

$$P_i = -\ln\left[\int w_i(E)\exp\left(-\int_L \mu(\mathbf{x},E)dl\right)dE\right].$$

To first order,

$$P_i \approx \int_L \mu(\mathbf{x},E_i)dl + error \tag{28}$$

Here E_i is the average detected energy in the ith layer. Thus P_i represents the line integral through the attenuation map at E_i. The error term represents the additional nonlinear contributions that cause beam hardening artifacts in polychromatic acquisitions. We can use the complete set of P_i to reconstruct approximate images of $\mu(\mathbf{x},E_i)$ for $i = 1,\ldots,N_{lay}$ corresponding to the energy-weighting achieved by the different layers. Examining the N_{lay} values of μ at each spatial position $\mathbf{x}$ potentially allows material discrimination, as will be seen in the next section.

The same approach can be used in the case of the single-channel color detection, except in this case, we first solve for an estimate of the layer-specific signals

$$\hat{\mathbf{N}}^{tot}(\mathbf{A}) = B^{-1}\overline{\mathbf{M}}^{Color}, \tag{29}$$

where we use the carat to indicate an estimated quantity. Then we define

$$P_i^{color} \equiv -\ln\left(\frac{\hat{N}_i^{tot}(\mathbf{A})}{\hat{N}_i^{tot}(\mathbf{0})}\right) \tag{30}$$

and the remaining analysis proceeds as in the multi-channel case.

2. *Simulations*

We performed numerical simulations to predict the ability of the classification approach to distinguish different metal stains that have been successfully used in electron microscopy and that are taken up by different biological targets. These stains are listed in table II and have absorption edge(s) in the 10-35 keV range. The simulated phantom consisted of 3 glass tubes with 0.4 mm internal diameter and 0.8 mm outer diameter. These tubes were assumed to be filled with 1%, 2% and 4% concentration of a given stain solution.

We chose the parameters of the simulation to match as closely as possible to the experimental parameters used in the actual synchrotron experiment to be described in the next section. The synchrotron spectrum assumed is shown in Fig. 2. Since this was a proof of feasibility experiment, we did not seek to push the limits of spatial resolution and used a relatively low-NA 2X lens and relatively thick scintillators. We simulated a dual-layer scintillator comprising a 100 micron front layer of LuAG doped with Ce and and 150 micron back layer of LYSO doped with Ce. The camera response spectrum was chosen to match that of the Prosilica GC1380CH used in the experiment. They are plotted in figure **??**.

The projection data were computed for these tubes containing the stain solutions based on the model above. We then solved for the P_i^{color} values at each detection pixel as described in in the previous section and reconstructed the images using the filtered back projection (FBP) algorithm. From the reconstructed images from the two layers, the mean attenuation value was computed over an ROI of size 0.02 cm^2 for each of the three tubes. Using this set of attenuation values for the two layers, one can plot the low-energy weighted attenuation values obtained from the first layer along the x-axis and the high-energy weighted attenuation values obtained from the second layer along the y-axis for different concentrations of a given stain. These values should fall along a straight line. Based on the slope of best fit line for each stain on this plot, one can compute the angular separation between the lines for various stain pairs. A higher angular separation indicates a better material discrimination in the image domain[7].

Stain	Biological Target	Absorption Edge (keV)
phosphotungstic acid (PTA)	Fibrin, collagen, connective tissue	10.2 keV (L3 edge)
phospohomolybdic acid (PMA)	Connective tissue	19.99 keV (K edge)
silver nitrate	Proteins, DNA reticula	25.51 keV (K edge)
indium chloride	Nucleic acids	27.94 keV (K edge)
molecular iodine	Cell nuclei	33.16 keV (K edge)

Table II: Stain solutions used

3. *Experiment*

We performed an experimental test of the feasibility of material classification using a multi-layer scintillator at Beamline 2-BM of the Advanced Photon Source (APS) at Argonne National Lab (ANL). We used a dual-layer scintillator detector comprised of a 100-micron layer of LuAG doped with Ce and a 150-micron layer of LYSO doped with Ce. These were glued together with epoxy. The lens employed was a 2X Mitutoyo. The light emitted by the detector was collected using a Prosilica GC1380CH with sensor dimensions 1360X1024 and a 6.45 um micron pixel size. Thus we had ~3.2 micron detection pixel size. We acquired 360 projection views spanning 180 degrees. We performed the acquisition on phantoms comprising glass tubes with 0.4 mm internal diameter and 0.8 mm outer diameter containing 1%, 2%, and 4% solutions of the stains listed in Table II. Note that the molecular iodine was dissolved in ethanol and the other stains were dissolved in water. We used the FBP algorithm to reconstruct the low- and high-energy weighted attenuation images from the P_i^{color} values calculated as described in Sec. II D 1. We also performed deringing on these reconstructed images using the ring-correction in polar coordinates (RCP) method[25].

III. RESULTS

A. Material decomposition

The calculated results for both the two-channel configuration with monochrome cameras and the one-channel configuration with color camera are given for test object 1 in Table III and test object 2 in Table IV. We observe that silver and molybdenum yield the best line-integral SNRs for the bending magnet spectrum, likely because their K edges are well matched to the mean

of the simulated bending magnet spectrum. Iodine offers much weaker performance as its K edge is not well matched to the spectrum. All the metals except tungsten, with its relative low-energy L edge, offer high SNRs for the undulator spectrum.

Focusing on silver, if we were to use an SNR cutoff of 5 as a threshold for acceptable quantitation performance, we see that we do not achieve that threshold for the first test object (50 microns of contrast) with the bending magnet in 1 s but we do achieve it with the undulator device, even with the single-channel configuration. For the second object (3mm of contrast and 3 mm of quartz), the threshold is achieved for bending magnet flux, for both the two-channel and single-channel configurations. The undulator SNR for the second object containing silver is so high that we could readily reduce the imaging time and still achieve a useful SNR. Since the SNR is expected to scale as the square root of flux for quantum limited measurements, we find we could achieve an SNR of 5 for test object 2 in approximately 1/660 of a second, which would allow for high-speed quantitative fluoroscopy or rapid quantitative material tomography.

Element	Two-channel (Mono) SNR		One-channel (Color) SNR	
	Bending Magnet	Undulator	Bending Magnet	Undulator
Ag	0.45	8.26	0.26	5.83
I	0.02	2.43	0.02	1.32
W	0.14	1.17	0.08	1.17
Mo	0.53	11.66	0.39	9.65
In	0.28	6.00	0.14	3.90

Table III: Phantom 1 (50 microns contrast in 3 mm water) contrast-agent SNR for 1 second of imaging at bending magnet and undulator fluxes.

Element	Two-channel (Mono) SNR		One-channel (Color) SNR	
	Bending Magnet	Undulator	Bending Magnet	Undulator
Ag	11.17	128.54	5.57	73.39
I	1.84	89.75	0.77	42.38
W	0.08	6.61	0.07	2.23
Mo	6.13	55.27	3.99	42.21
In	8.66	126.80	4.04	66.33

Table IV: Phantom 2 (3 mm contrast in 3 mm quartz) contrast-agent SNR for 1 second of imaging at bending magnet and undulator fluxes.

B. Material classification

A typical reconstruction is shown in Fig. 4 showing tubes containing 4%, 2% and 1% solutions of PTA in water. Slight contrast differences are visible between the two images but nothing that allow visual material classification. However, Fig. 5 shows a more quantitative analysis of the attenuation values found in the two layer images for the various elements and concentrations.

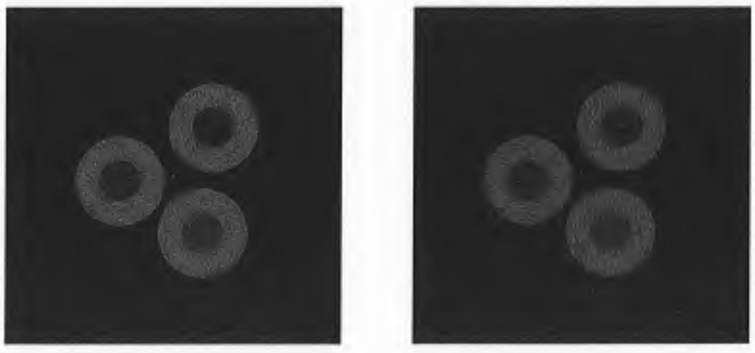

Figure 4: Reconstructed phantom slices using the signal from the two scintillation layers.

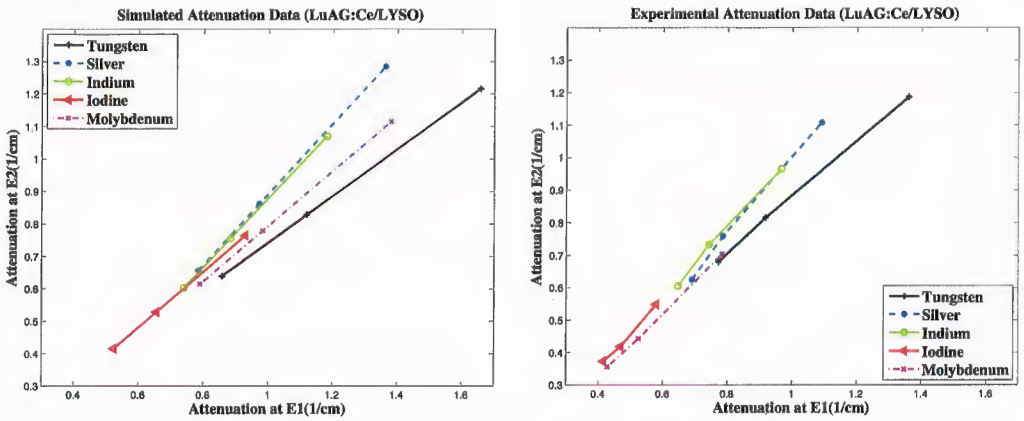

Figure 5: Dual layer attenuation values for the various stains considered.

Each point represents the mean value in a tube lumen for a tube of given element and concentration. The three concentration points for a given element are connected by a line. By fitting a line passing through the origin to each such triplet of points, it is possible to calculate the angle between the different stain pair lines. Table V lists the calculated angular separation in the simulated and experimental data.

Stain Pair	Angular Separation (degrees)	
	Simulation	Experiment
Ag - W	11.6	9.4
W - In	10.7	7.4
Ag - Mo	7.1	5.3
W - Mo	4.4	4.1
Ag - I	6.7	2.5
In -I	5.8	0.5
W - I	4.9	6.9

Table V: Angular separation between various stain solution pairs for synchrotron spectrum using a LUAG:CE(100 μ)/LYSO(150 μ) dual-layer detector

The agreement between simulation and experiment is generally good, with the simulation typically overestimating the angular separation relative to what was observed. The discrepancies are most severe in the case of the iodine pairs. This suggests that the source of the discrepancy is likely related to inaccurate modeling of the synchrotron spectrum, especially the distribution at high energies, which would most affect iodine, as it has the highest absorption edge of all the stains considered. There could also have been some precipitation of the solutions in the experiment, leading to lower concentrations in the measured tubes than were assumed in the simulations. Another source of discrepancy could be the unknown hydration level of the PMA and PTA stains. We did not know the exact water concentration in those stains at the time of making the solutions. The simulated data assumes that PMA and PTA had 21.7% and 10.5% water respectively (based on manufacturer's data).

We see that for this scintillator construct and synchrotron spectrum, the silver-tungsten and indium-tungsten pairs have the greatest separability.

IV. DISCUSSION AND CONCLUSIONS

We have demonstrated that a dual-layer, dual-color scintillator construct, originally proposed by Martin *et al.* to increase sensitivity in synchrotron imaging, can also be used to perform material quantification and classification when coupled with polychromatic illumination. We considered two different approaches to data handling: a data-domain material decomposition

whose estimation performance could be characterized by the CRLB formalism but required careful calibration and an image-domain material classification approach that was more robust to calibration errors. The data-domain analysis indicated that useful levels of SNR (>5) could be achieved in one second or less at bending magnet fluxes for relatively large amounts of contrast (several mm path length, such as in a fluid flow experiment) and at undulator fluxes for small amount of contrast (tens of micron path length, such as an angiography experiment). The tools introduced could of course be used to study and optimize parameters for a wider range of potential applications. In particular, while we considered two different fixed spectra here, it would be possible to further improve the performance for a given metal contrast agent by using the tools presented here to tailor the spectrum through filtering or other adjustments. The image domain approach was analyzed in terms of its ability to distinguish different elemental stains by characterizing the angle between the lines traced out in a two-dimensional space of effective attenuation coefficient in the front and back layer images. This approach was implemented at a synchrotron and the results agreed reasonably well with simulation predictions.

We considered two different optical setups for recording the scintillator images. The first, as in Martin *et al.*, involved using a dichroic mirror to separate the emissions of the two layers into two different optical channels, each with a microscope objective focused on the appropriate later. Since scintillator thickness in microscopic x-ray imaging must match the depth of focus of the objective lens, this allows a potential doubling of the effective thickness and thus stopping power of the system. We also considered a simpler configuration in which a single color camera views the dual-layer scintillator through a single objective lens. Now the combined thickness of the two layers must match the depth of focus of the lens so SNR will inevitably suffer. A second potential source of SNR degradation in this configuration is the need to demultiplex the received color signals to identify the signal from each layer. This has the potential to amplify the additive electronic noise in the camera. However, this effect can be minimized by choosing scintillators whose emissions are well separated, such as the LuAG:Ce and LYSO:Ce pair used here. We studied the contribution of the "color penalty" to our SNR degradation by calculating the SNR obtained when using the color camera but ignoring the constraint that the summed layer thickness match the DOF; thus the dual layer scintillator was the same as in in the two-channel monochrome camera case, but was viewed by the color camera. We found that the reduction in SNR due to color demultiplexing was almost always less than 1%.

We focused in this paper on application to dynamic synchrotron imaging since only synchrotrons have the flux necessary to perform high-speed, high-resolution imaging with material quantification and classification. However, for slower processes or static imaging, the proposed configuration could be used in a benchtop x-ray microscopy system, which routinely use scintillator-microscope combinations to achieve micron scale resolution. The detailed analysis of sensitivity in a tube-based system is beyond the scope of the present paper but could be readily carried out using the CRLB formalism used here.

V. ACKNOWLEDGEMENTS

We would like to thank Subha Rajamani for her help in preparing the stain solutions and Jayasai Rajagopal for help in the CRLB analysis. We would like to acknowledge support from NIH grants R01EB017293 and R01CA134680.

[1] J.C. Andrews, F. Meirer, Y. Liu, Z. Mester, P. Pianetta, "Transmission X-ray microscopy for full-field nano imaging of biomaterials," Microsc. Res. Tech. 74(7), pp. 671-81, 2011.

[2] K.C. Cheng, X. Xin, D.P. Clark, P.J. La Riviere, "Whole-animal imaging, gene function, and the Zebrafish Phenome Project," Curr. Opin. Genet. Dev. 21(5), pp. 620-9, 2011.

[3] J.F. Adam, S. Bayat, L. Porra, H. Elleaume, F. Estève, P. Suortti, "Quantitative functional imaging and kinetic studies with high-Z contrast agents using synchrotron radiation computed tomography," Clin. Exp. Pharmacol. Physiol. 36(1), pp. 95-106, 2009.

[4] A. Koch, C. Raven, P. Spanne, and A. Snigirev. "X-ray Imaging with Submicrometer Resolution Employing Transparent Luminescent Screens," J. Opt. Soc. Am. A 15(7), pp. 1940, 1998.

[5] T. Martin, P. Douissard, M. Couchaud, A. Cecilia, T. Baumbach, K. Dupre, and A. Rack. 'LSO-Based Single Crystal Film Scintillator for Synchrotron-Based Hard X-Ray Micro-Imaging', IEEE Trans. Nuc. Sci., 56(3), pp. 1412-418, 2009.

[6] P. Stenner, T. Berkus and M.Kachelriess, "Empirical dual energy calibration (EDEC) for cone-beam computed tomography," Med. Phys. 34(9), pp. 3630-3641, 2007.

[7] A.N. Primak, J.C. Ramirez Giraldo, X. Liu and C.H. McCollough, 'Improved dual-energy material discrimination for dual-source CT by means of additional spectral filtration', Med. Phys., 36(4), pp. 1359-1369, 2009.

[8] B.J. Heismann, S. Wirth, S. Janssen and Spreiter, "Technology and image results of a spectral CT system," Proc. SPIE Med. Imag. 5368, pp. 52–9, 2004.

[9] D.P. Chakraborty and G.T. Barnes, "An energy sensitive cassette for dual-energy mammography," Med. Phys. 16, pp. 7-13, 1989.

[10] "Dual energy CT in clinical practice," T.R.C. Johnson, C. Fink, S.O. Schönberg, M.F. Reiser (Eds.), Springer-Verlag, Berlin Heidelberg, 2011.

[11] R.E. Alvarez, and A. Macovski. "Energy-selective Reconstructions in X-ray Computerized Tomography," Phys. Med. Bio. 21(5), pp. 733-44, 1976.

[12] E. Roessl and C. Hermann, "Cramer–Rao lower bound of basis image noise in multiple-energy x-ray imaging," Phys. Med. Bio. 54, pp. 1307-1318, 2009.
[13] T.R.C. Johnson *et al.*, "Material differentiation by dual energy CT: initial experience," Eur. Rad. 17(6), pp. 1510-1517, 2007.
[14] D. Rigie and P.J. La Riviere,'Multiple-energy micro-CT using multi- layerd, multi-color,thin-film scintillators', Proc. IEEE NSS/MIC, pp. 4009-4012, 2011.
[15] D. Modgil, D. Rigie, S. Wang, X. Xiao, P.A. Vargas and P.J. La Riviere, "Basis element decomposition with spectral microCT using multi-layered, multi-colored scintillation detectors," Proc. IEEE NSS/MIC Proc., pp. 3713-3716, 2012.
[16] http://www.nist.gov/pml/data/xraycoef/
[17] B.R. Whiting, "Signal statistics in X-ray computed tomography," Proc. SPIE, 4863, pp. 53-60, 2002.
[18] I.A. El Bakri and J.A. Fessler, "Efficient and accurate likelihood for iterative image reconstruction in x-ray computed tomography," Medical Imaging 2003: Image Processing, SPIE 5032, pp. 1839-1850, 2003;
[19] B. R. Whiting, P. Massoumzadeh, O. A. Earl, J. A. O'Sullivan, D. L. Snyder, and J. F. Williamson, "Properties of preprocessed sinogram data in x-ray computed tomography," Med. Phys. 33, pp. 3290–303, 2006; http://dx.doi.org/10.1118/1.2230762.
[20] J. A. Fessler, "Statistical image reconstruction methods for transmission tomography," Handbook of Medical Imaging, J. M. Fitzpatrick and M. Sonka, Eds. Bellingham, WA: SPIE Press, 2, pp. 1-70, 2000.
[21] J. Xu; E.C. Frey; K. Taguchi; B.M.W. Tsui, "A Poisson likelihood iterative reconstruction algorithm for material decomposition in CT," Proc. SPIE 6510, Med. Imag. 2007: Physics of Medical Imaging, pp. 65101Z, 2007; doi: 10.1117/12.713727.
[22] J. Noh, J.A. Fessler, P. Kinahan, "Statistical Sinogram Restoration in Dual-Energy CT for PET Attenuation Correction," IEEE Trans. Med. Imag. 28(11), pp. 1688–1702, 2009; doi:10.1109/TMI.2009.2018283.
[23] S. Kay, 'Fundamentals of Statistical Signal Processing, Volume I: Estimation Theory (v. 1),' Prentice Hall, 1998.
[24] M. Sánchez del Río and R. J. Dejus., "XOP 2.1: A new version of the X-ray optics software toolkit," Synchrotron Radiation Instrumentation: Eighth International Conference, T. Warwick (Eds.), American Institute of Physics, pp. 784-787, 2004.
[25] D. Prell, Y. Kyriaku and W.A. Kalendar, "Comparison of ring artifact correction methods for flat-detector CT'," Phys. Med. Bio. 54, pp. 3881-3895, 2009.